

## 1. Process optimization

Additional purification of M13 clones is recommended to ensure reproducibility of nanofoam structures. Figure S1 reports a schematic of standard M13 preparations after typical centrifugation and PEGylation purification steps. As DNA and residual extracellular proteins are also negatively charged it is anticipated that these components also participate in the templating process if they are not removed from the M13 preparations through additional DNase and dialysis steps. Additionally, the incorporation of EDTA in the dialysis water is imperative to avoid excessive M13 aggregation due to the affinity divalent cations and the M13 mutants utilized in this experiment.

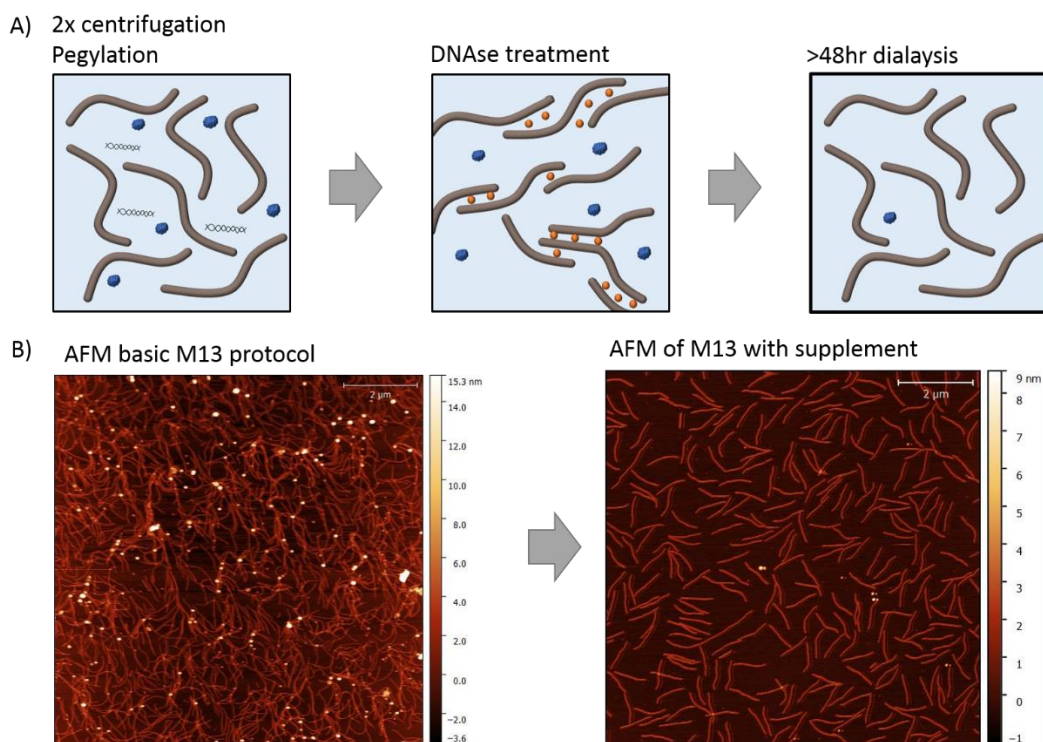
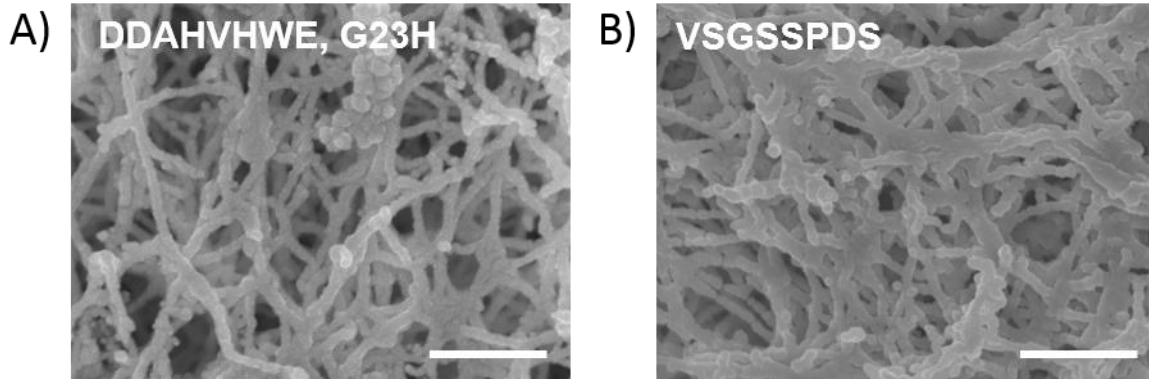


Figure S 1: A) Schematic of additional dialysis DNase purification steps B) AFM images of EEAE clones before and after additional purification

## 2. M13 clone design and selection

Several M13 clones were tested for their ability to complete protein based sensitization sufficient for electroless metal plating. Each demonstrated the ability to template metal as demonstrated in S2.



*Figure S 2 M13 clones including p8 inserts alternative to E-E-A-E successfully templated metal nanofoam materials as demonstrated via SEM images of nanofoams composed of (A) a histidine rich clone<sup>1</sup> and (B) a serine rich clone<sup>2</sup>. Both clones were templated at a density of  $2 \times 10^{13}$  phage per ml for 20 minutes with nickel electroless deposition solution. Scale bar represents one micron.*

In order to construct nanofoams with clone specific architectures, we identified an M13 clone candidate with inserts containing acids which would differ in character from the EEAE clone which would presumably display a lower affinity to divalent cations. As such we focused on clones with mainly bulky non-polar / non-charged residues. Additionally, we utilized candidates which displayed representation in high throughput sequencing data above 4 counts per million reads from a p8 library described previously.<sup>3</sup> The following p8 inserts and respective sequences were selected and cloned via site-directed mutagenesis (QuikChange II Site-Directed Mutagenesis, Agilent).

<b>p8 insert (nucleotide sequence)</b>	<b>Resulted in stable clone</b>
<b>GEYFQYDQ (GGTGAGTATTTTCAGTATGATCAG)</b>	Yes
<b>GEYFNYDE(GGGGAGTATTTTAATTATGATGAG)</b>	Yes
<b>GYADTYYE (GGTTATGCTGATACTTATTATGAG)</b>	No
<b>ETSYFYDT (GAGACGAGTATTTTATGATACG)</b>	Yes
<b>DPYYFNDT (GATCCTTATTATTTAATGATACG)</b>	No
<b>DYFEYGSP (GATTATTTGAGTATGGGTCTCCG)</b>	No
<b>DFSTYYDQ (GATTTTAGTACGTATTATGATCAG)</b>	No

Of the candidates chosen, the clone E-T-S-Y-F-Y-D-T demonstrated the highest M13 amplification yield. Furthermore, affinity for the clones E-T-S-Y-F-Y-D-T and E-E-A-E with divalent cations (magnesium) was further examined via centrifugation in the presence of 100mM magnesium chloride (Figure S3) and 10mM and 100mM calcium chloride (Figure S4). In a side by side comparison, the addition of magnesium salts enabled complete removal of E-E-A-E clones from solution via centrifugation. Alternatively, only half of the virions were removed after salt addition and centrifugation in the E-T-S-Y-F-Y-D-T clone (Figure S3). Similarly, the addition of 10mM calcium chloride and subsequent centrifugation removed close to 75 % of the E-E-A-E clones from solution and about 30 % of the E-T-S-Y-F-Y-D-T clones (Figure S4). Though beyond the scope of this study, this behavior of the E-T-S-Y-F-Y-D-T clone may be attributed to the reduction of charged groups in the p8 coat and increase in bulky aromatic groups on the exposed terminus as compared to the E-E-A-E clone.

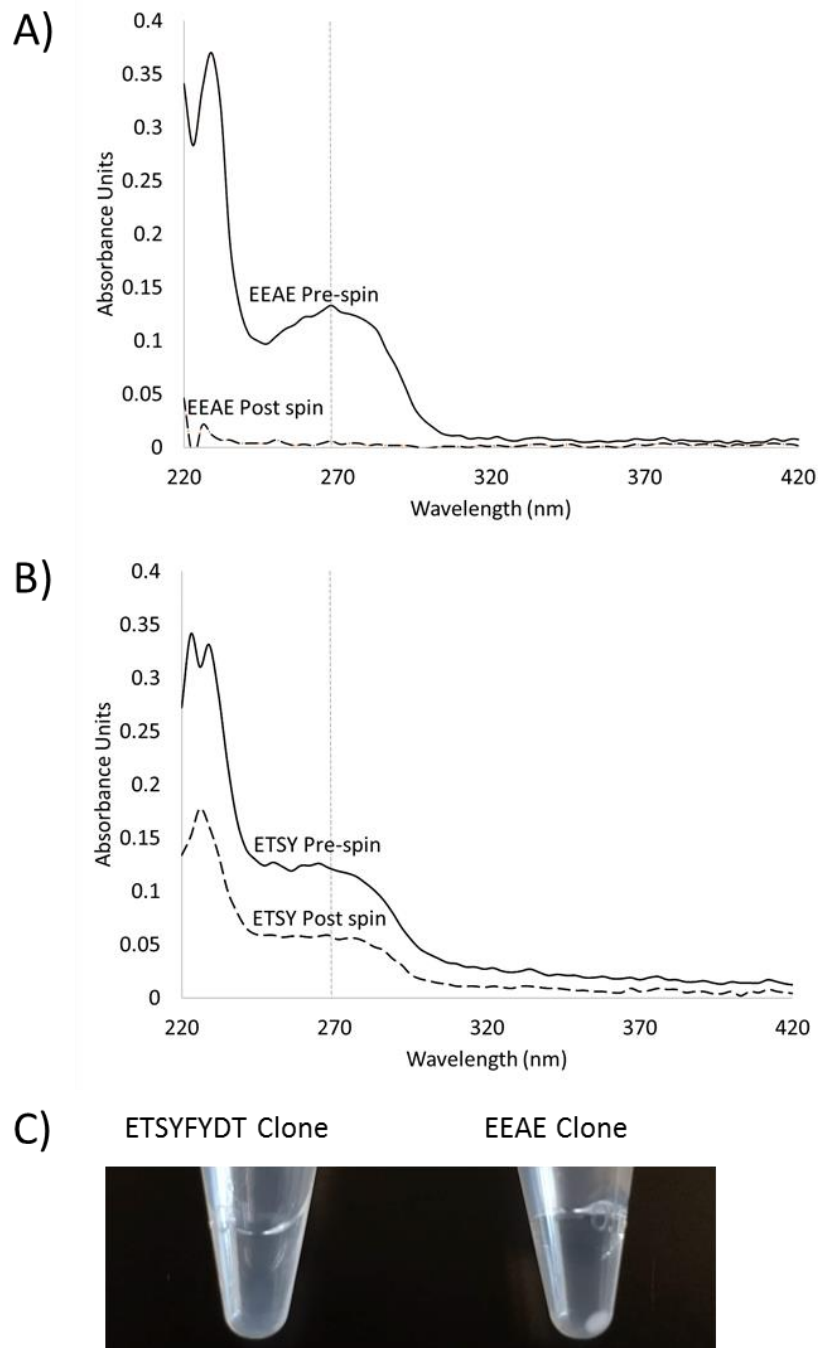


Figure S 3: A comparison of the UV-visible absorbance of M13 solutions of the clones (A) EEAE and (B) ETSY before and after centrifugation (10,000 rpm for 5 minutes) in the presence of the salt magnesium chloride (100mM). Clones were both at the concentration  $1.7 \times 10^{13}$  pfu/ml. 269 nanometers, the wavelength utilized to determine the concentration of M13 phage in solution, is depicted as a grey horizontal line. The visible pellet of aggregated EEAE clones as compared to the ETSY clones after centrifugation is also presented (C).

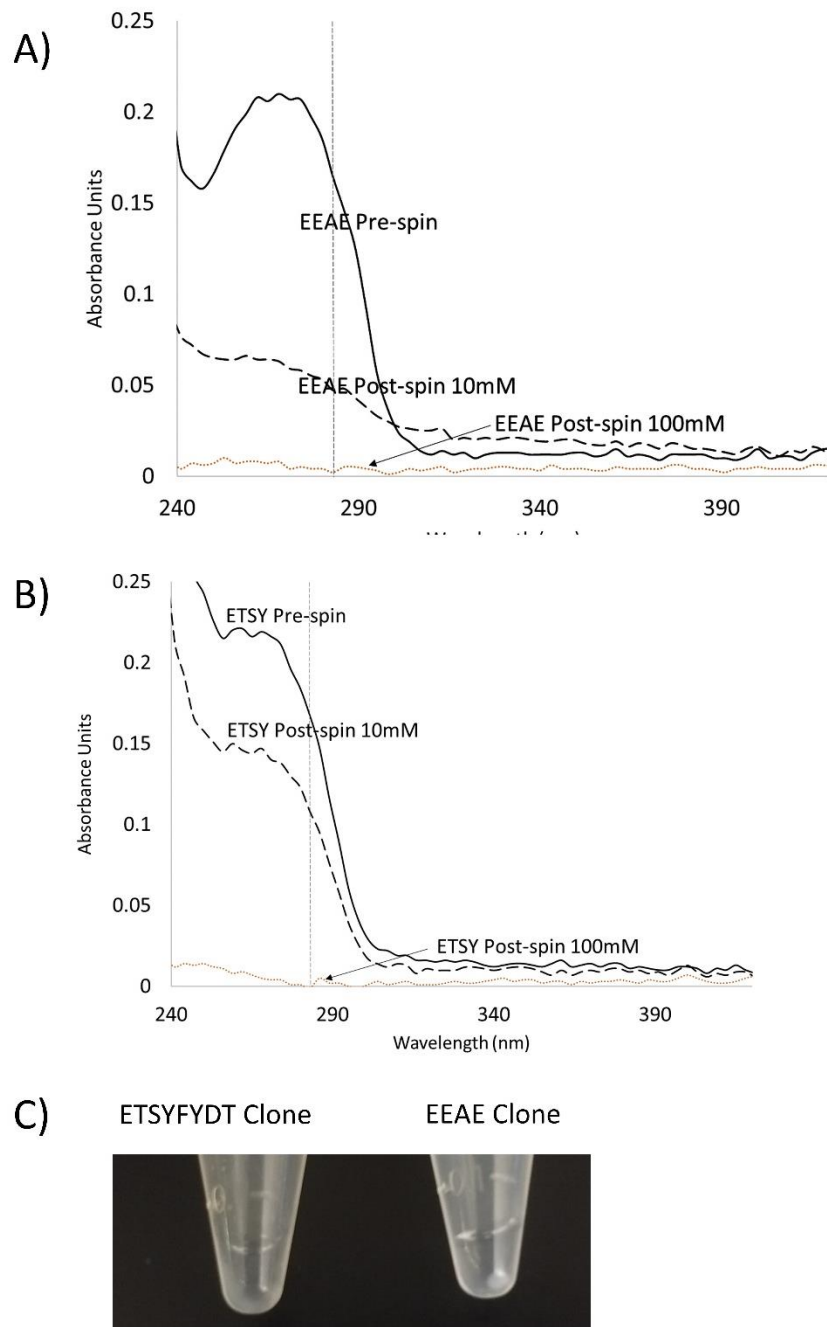
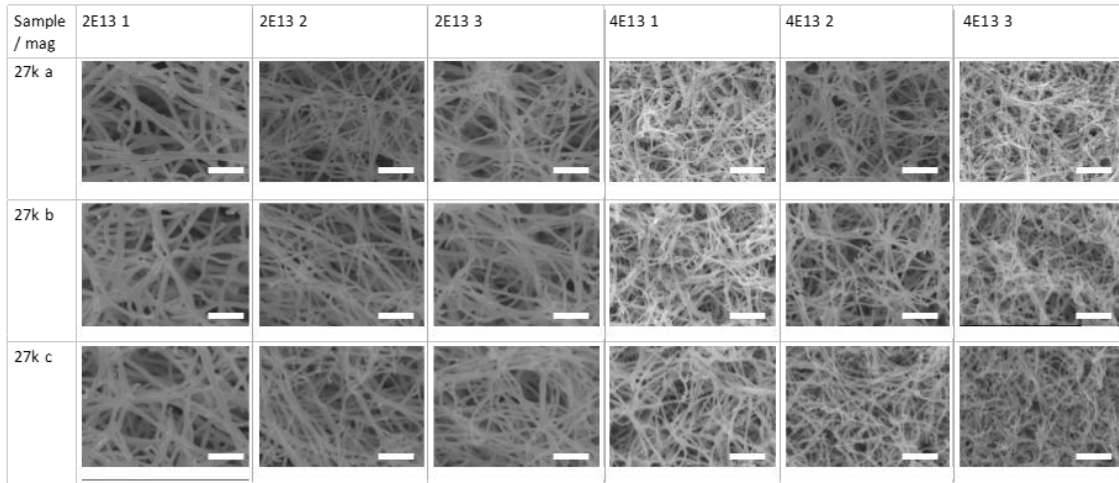


Figure S 4 A comparison of the UV-visible absorbance of M13 solutions of the clones (A) EEAE and (B) ETSY before and after centrifugation in the presence of the salt calcium chloride (10mM and 100mM centrifuged at 10k rpm for 1 and 10 minutes respectively). Clones were both at the concentration  $1.7 \times 10^{13}$ . 269 nanometers, the wavelength utilized to determine the concentration of M13 phage in solution, is depicted as a grey horizontal line. The visible pellet of aggregated EEAE clones as compared to the ETSY clones after centrifugation is also presented (C)

### 3. Architectural quantification

DiameterJ was utilized to quantify the effects of altered template density on nanofoam architecture including both fiber diameter and the intersection density of fibers. While caution should be noted when interpreting data in a 2D format from 3D samples, care was taken to minimize depth of field disparities between samples. The same SEM settings, including magnification, were used on all samples and, each image was treated with the same equalization and contrast adjustments. Additionally, reported diameter and intersection densities were the result of averaging 3 randomly selected positions on each of 3 separate samples. S3 depicts the SEM images utilized in analysis as well as a sample segmented image.

A)



B)



C)

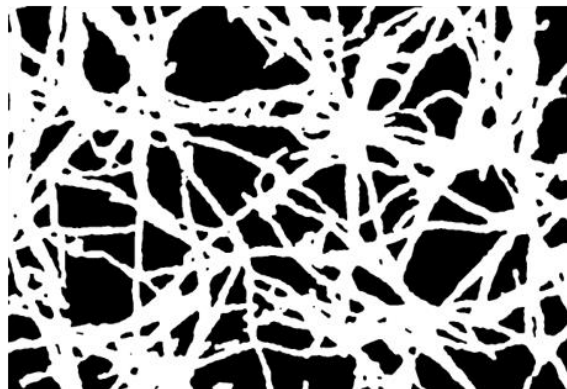


Figure S 5: (A) Raw SEM images collected for image analysis, scale bars represent one micron (B) Sample of  $2 \times 10^{13}$  segmentation (C) Sample of  $4 \times 10^{13}$  segmentation

#### 4. Growth kinetics of nanofoam struts

Growth curves for the nanofoams were constructed from SEM image analysis indicating control on the resolution on an estimated 20 nanometer scale. Nanowire diameters for 2-3 images per time point spanning 2 hours of exposure to electroless solution were measured via imageJ. Averages were taken for each image and then combined to represent the overall average at each timepoint revealing control over the range of 100-300nm diameters on roughly a 20nm resolution. Representative images utilized in this analysis as well as a growth curve for Ni nanonetworks formed with sodium hypophosphite reported in S2.

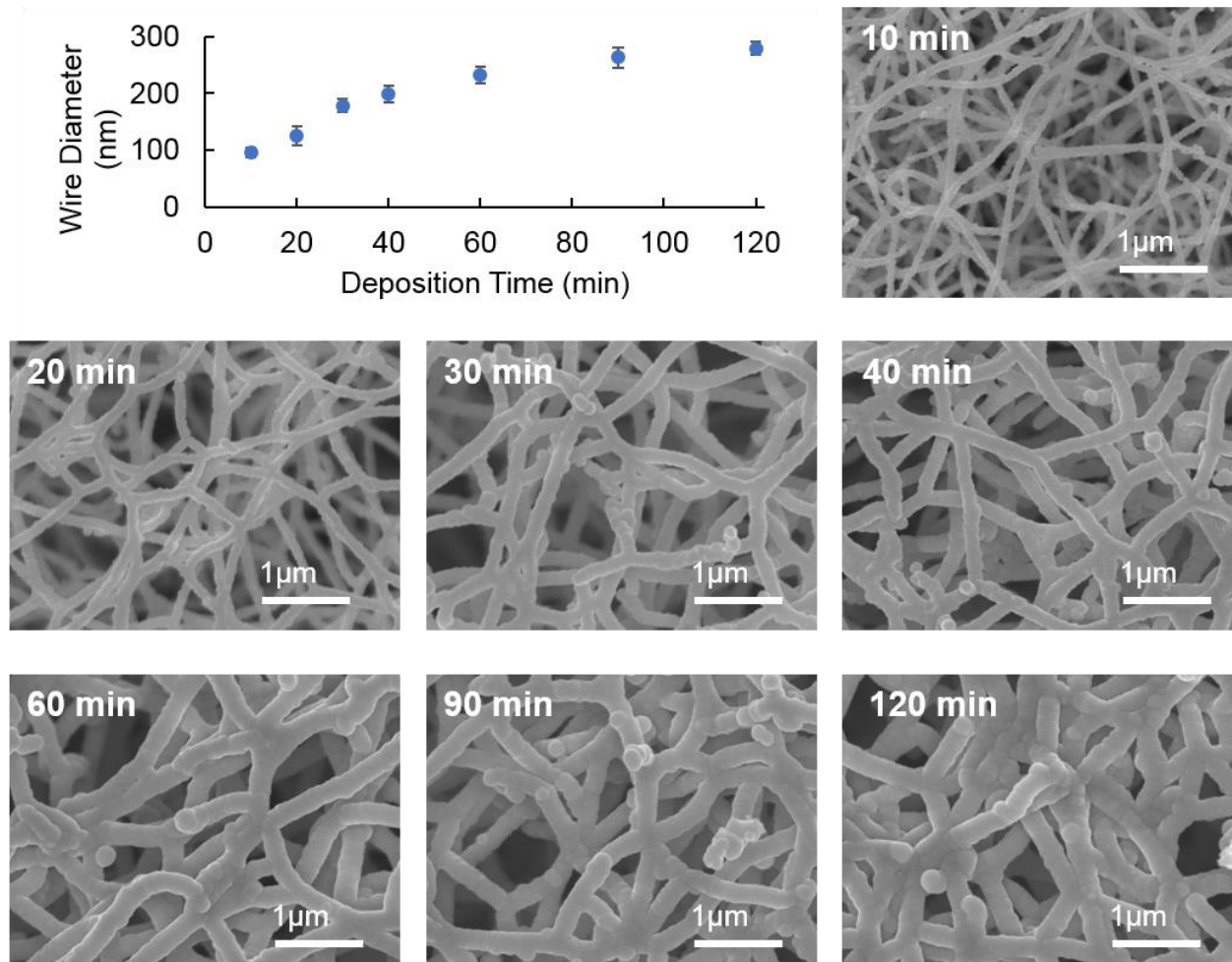


Figure S 6: Plot of nanowire diameter with respect to time spent in Ni electroless deposition bath with sample images of each timepoint.

## 5. Monometallic nanofoam characterization

Monometallic nanofoams were formed utilizing the processes described in the experimental methods section. The deposition times required to achieve nanofoams of comparable strut thickness varied from minutes to hours as deposition processes for different metals occur at different rates. This disparity in deposition rate likely contributed to the increased broadening of the nickel nanofoam XRD peak as compared to the sharper copper patterns reported in S7. While the electroless deposition process proceeds in a reducing environment, the drying process was carried out under air. It is likely that the copper oxide detected via XRD is a result of surface oxidation during this drying step.

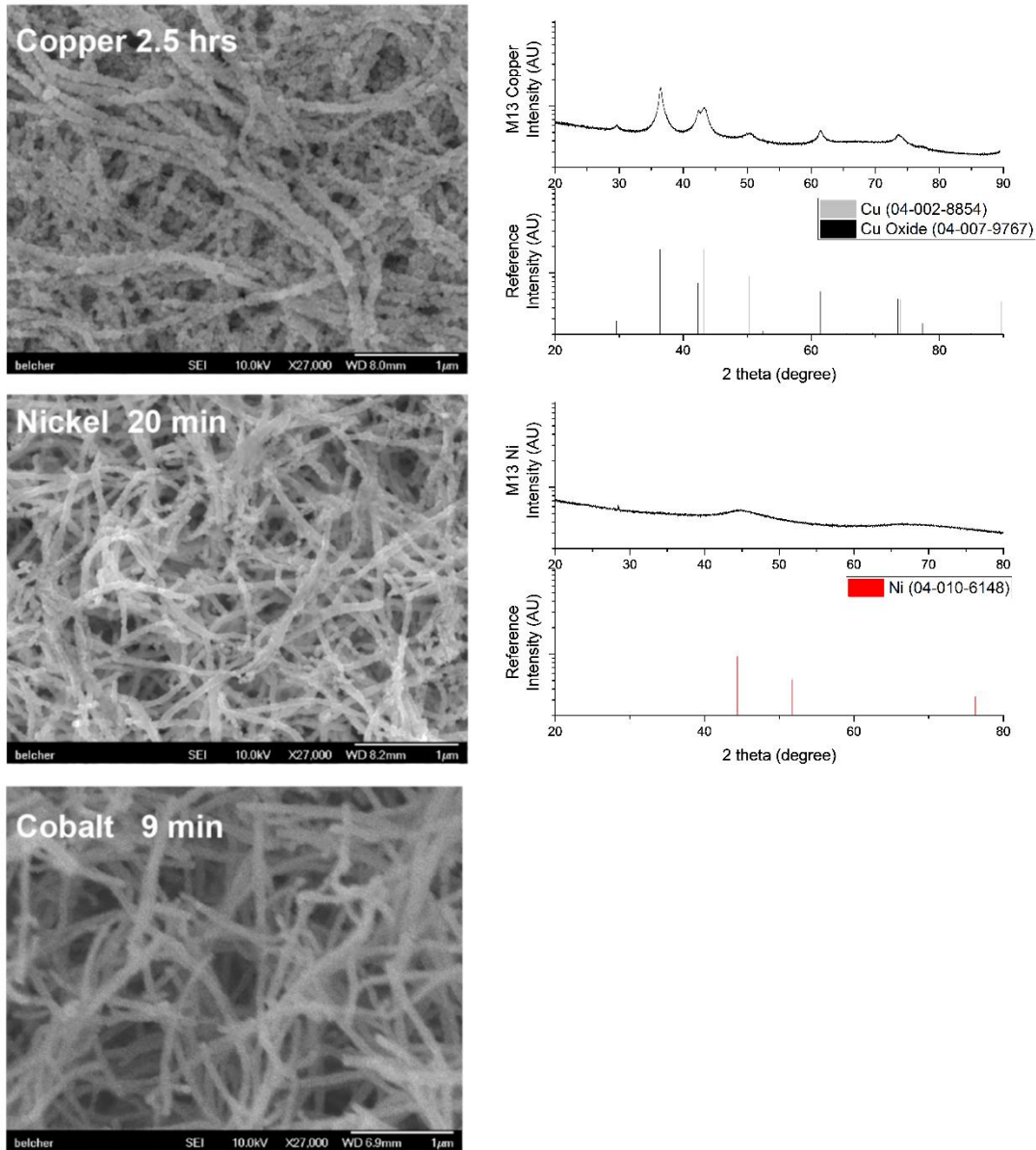


Figure S 7: Sample TEM images of monometallic nanofoams and respective XRD patterns preannealing. XRD graphs are presented on a log scale from 20k counts to 925k reference intensities are scaled to the maximum peak detected. Cobalt fluorescence from the X-ray source precluded cobalt XRD analysis.

## 6. Multimetallic nanofoam characterization

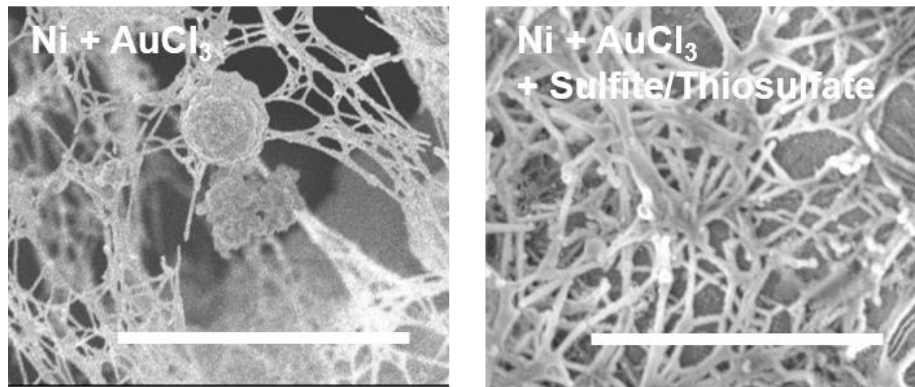


Figure S 8: Nickel nanofoams which have undergone gold deposition with (right) and without (left) the presence of sulfite/thiosulfate in the AuCl deposition solution. Scale bar is 10 microns

### Comparison of bimetallic copper and gold nanofoams:

As depicted in S10 panel C, the copper-nickel nanofoam exhibited a subpopulation of nanowires which demonstrated lower copper loading. This subpopulation was not apparent in gold coated wires. As the low copper loaded nanowires were typically smaller than the core-shell copper-nickel wires, this subpopulation of nanowires was located within presumably transport limited regions of the nanofoam. While further studies would be required to definitively explain this phenomenon, we speculate that the copper deposition mechanism is more sensitive to transport limitations in the deposition of the secondary metal due to the relatively lower copper concentration in the copper deposition solution (1.6mM) as compared to the gold deposition solution (10mM).

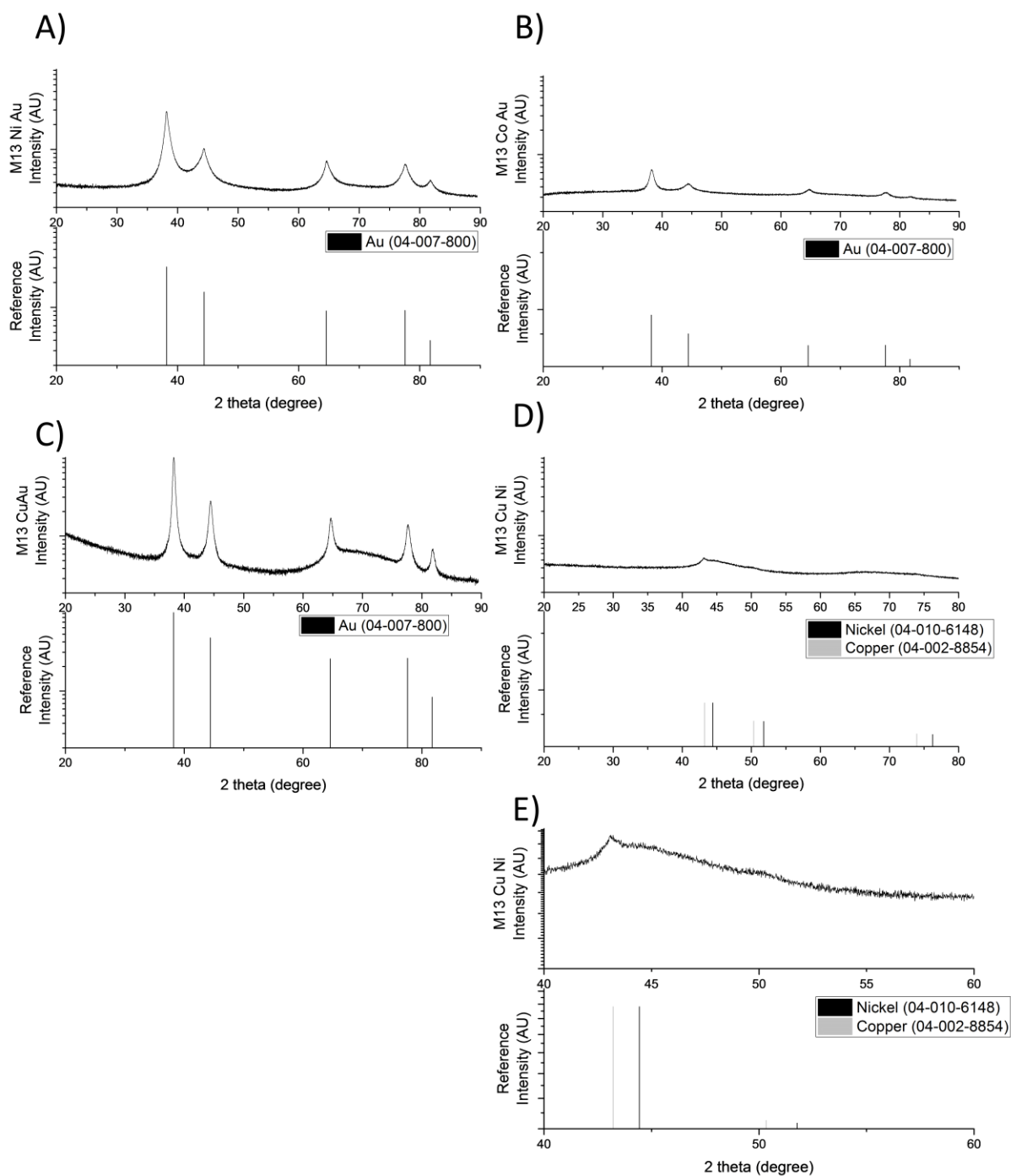


Figure S 9: Corresponding XRD patterns for multimetallic nanofoams depicted in Figure 3. XRD graphs are presented on a log scale from 20k counts to 925k reference intensities are scaled to the maximum peak detected. Gold patterns are clearly observed in nanofoams after gold treatment as reported in (A) nickel-gold nanofoam corresponding to 63% gold 37% nickel (B) cobalt-gold nanofoam corresponding to 36% gold 64% cobalt and (C) copper-gold nanofoam corresponding to over 99% gold. Significant peak broadening, observed in monometallic nickel nanofoams was also observed in the copper-nickel nanofoam corresponding to 32% copper and 68% (D), although the most prominent copper peak can be detected (E). All referenced atomic content was characterized EDS and reported in Figure 3.

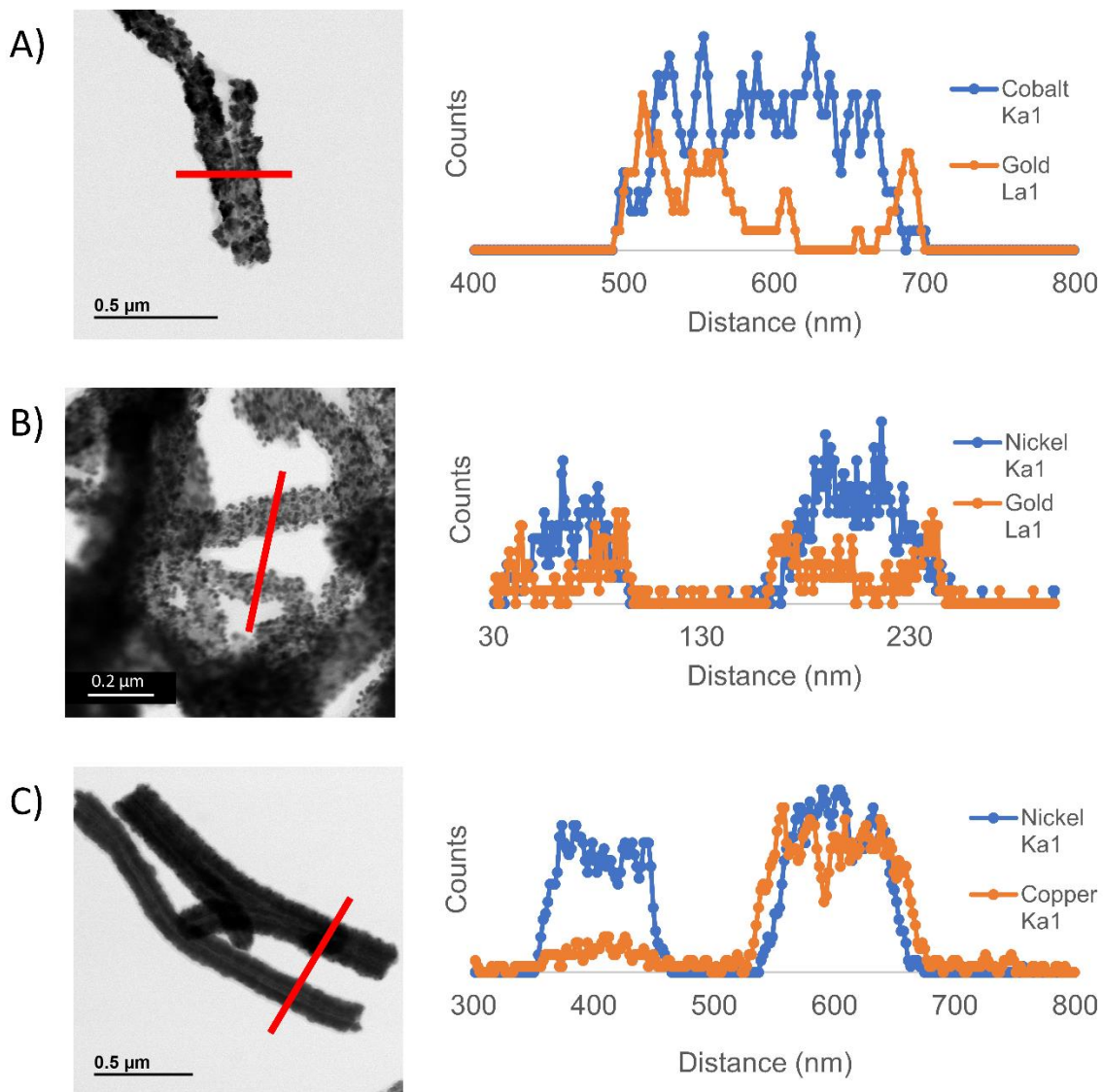
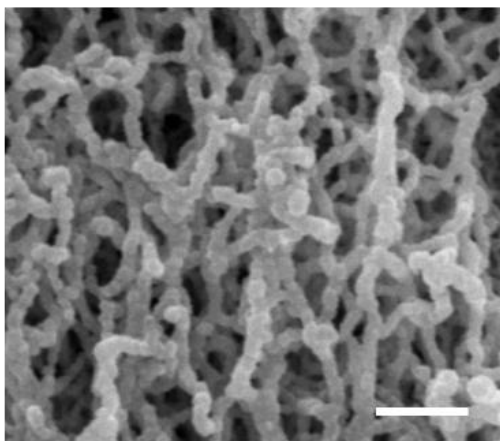
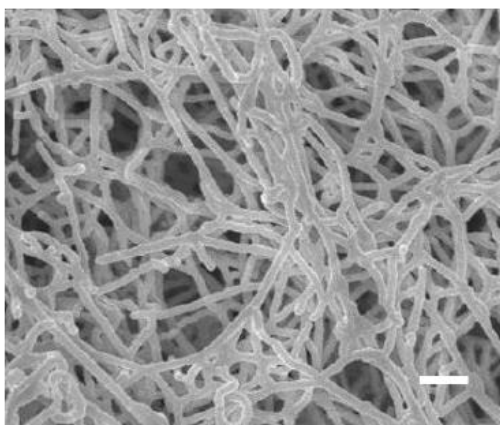
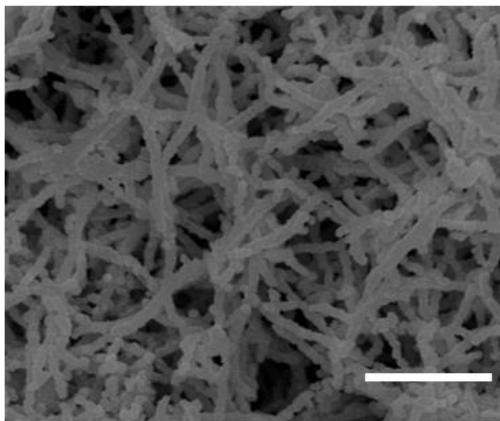


Figure S 10: Multimetallic nanofoam structures imaged via TEM (A) cobalt sample after gold deposition treatment (B) nickel sample after gold deposition (C) nickel sample after copper deposition. Panel (C) depicts two nanowires to report both the core-shell copper-nickel nanowires and the subpopulation of smaller, lower copper content wires.

A)



B)

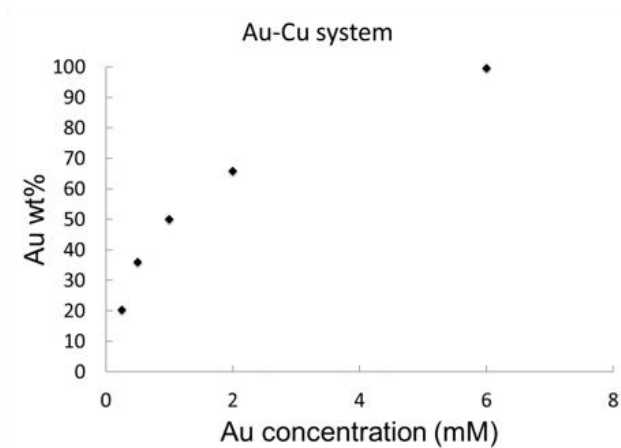
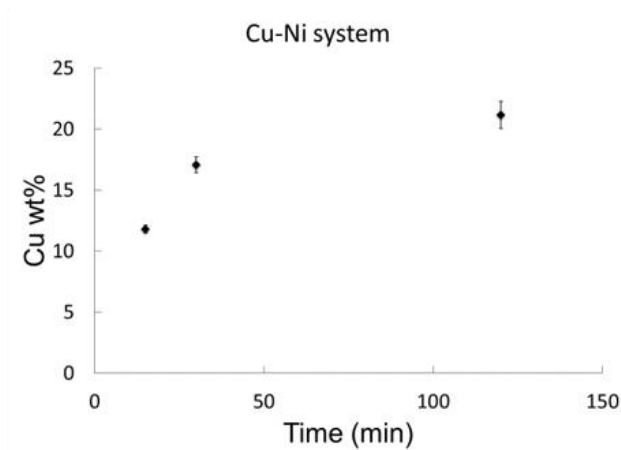
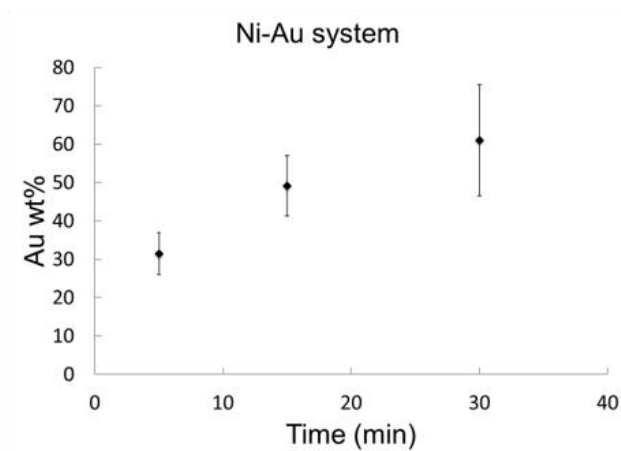


Figure S 11: (A) Representative images of nanofoams after two successive treatments of metal deposition. Scale bar depicts 1 micron. (B) Relationship between secondary metal incorporation via wt% into the resulting nanofoam. Error bars in the Au-Ni system correspond to a sample size of 3 nanofoams per data point. Data points in the Cu-Ni and Au-Cu system correspond to one sample per point, error bars for these materials depict uncertainty in wt% measurements.

Table S 1: Crystal sizes in biotemplated vs non biotemplated control samples. XRD patterns utilized in calculation are presented in Figure 4 and S6.

Ni phage template as synthesized										
hkl (ref 04-004-8868)	111	200	220							
2 theta	44.5	51.9	76.3							
Xl size (nm)	1.2	n/a	n/a							
HT Ni phage template										
hkl (ref 04-004-8868)	111	200	220							
2 theta	44.5	51.9	76.3							
Xl size (nm)	7.8	8	9.2							
HT Ni no template										
hkl (ref 04-004-4588)	210	121	201	220	31	112	122	301	401	332
2 theta	37.1	38.2	40.3	44.3	46	47	53.1	57.1	76.3	83.4
Xl size (nm)	43.6	35.5	25.9	23.4	32.5	32.5	52.6	31.1	44.1	30.4

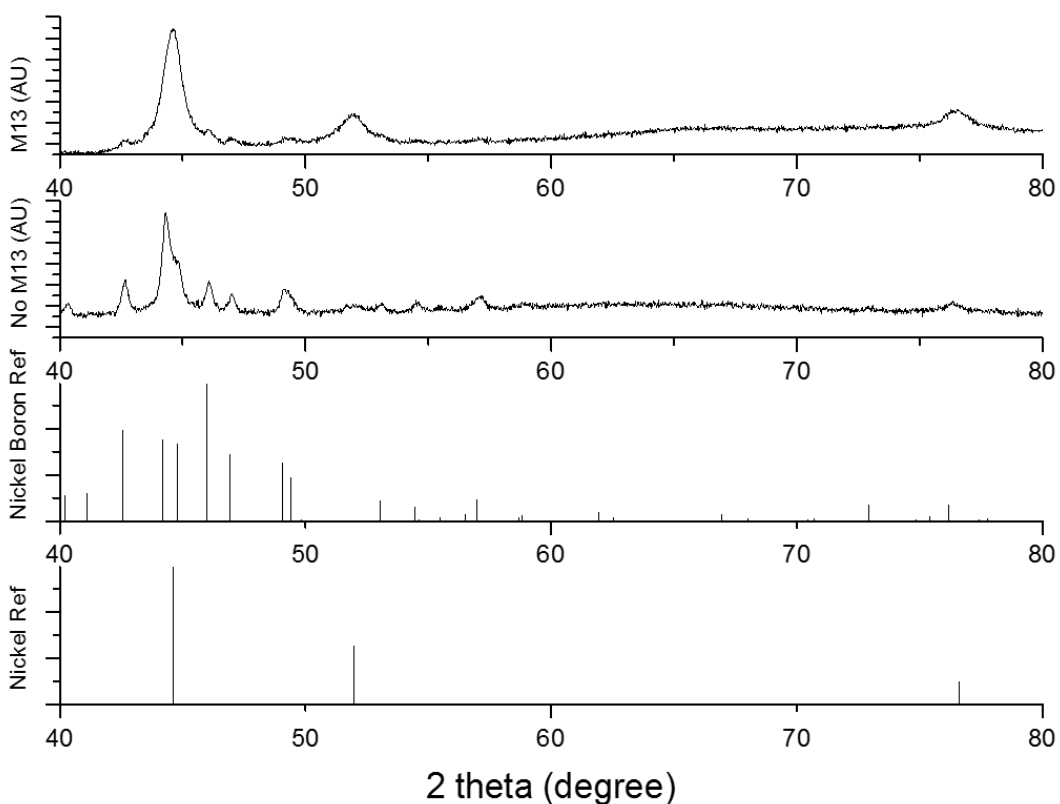


Figure S 12: Full XRD patterns of heat treated nickel samples with and without phage templated utilized in crystal size calculation. Scans are reported to 60 degrees 2 theta in figure 4. XRD graphs are presented on the same log scale and reference intensities are scaled to the maximum peak detected

Assumptions in crystal size calculations:

HSP software was used to calculate crystal sizes via the Scherrer equation. As both biotemplated and non-biotemplated samples were fabricated via identical electroless deposition solutions it was assumed that shape factor remained unchanged between template and non-biotemplated samples in crystallite size analysis. Shape factor value was taken to be 0.94 for that of spherical crystallites with cubic symmetry.

## 7. Surface area characterization

### Theoretical surface area

$$\text{Theoretical surface area} = \frac{2\pi r l}{\pi r^2 l \rho_M} = \frac{2}{r \rho_M}$$

$l$  = length

$r$  = radius

$\rho_M$  = density of metal (Nickel = 8.91g/cm<sup>3</sup>, Copper = 8.96g/cm<sup>3</sup>)

Theoretical surface area Ni or Cu = 4.5 – 1.5 m<sup>2</sup>/g for diameters from 100-300 nm

### BET

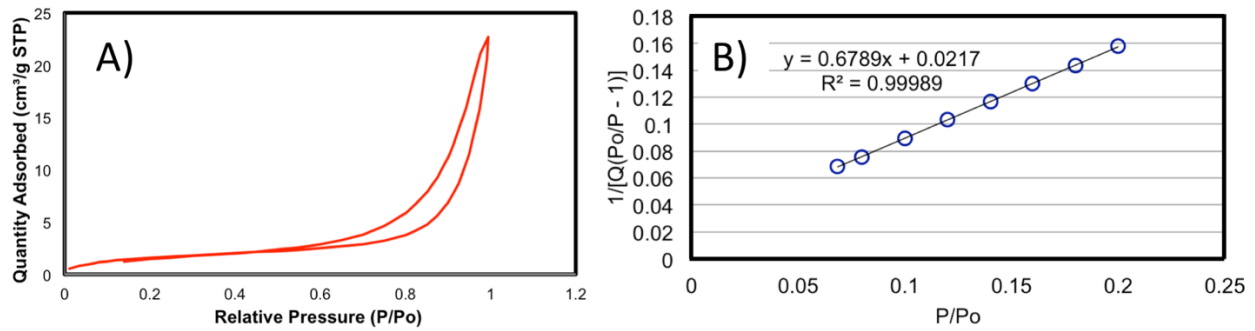


Figure S 13 Measuring the surface area of Nickel nanowires using Brunauer-Emmett-Teller analysis. A nitrogen adsorption curve is shown in (A). A BET plot is graphed in (B)

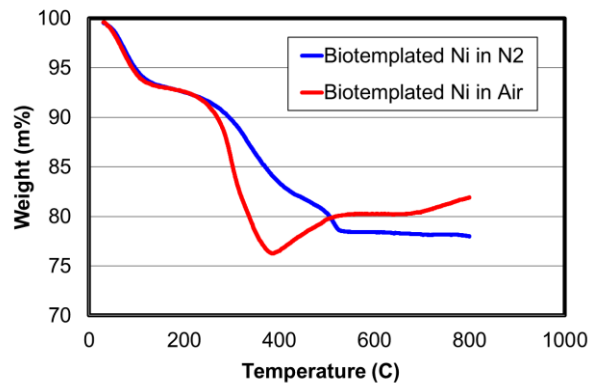


Figure S 14: Thermogravimetric analysis of M13 (EEAE) nickel nanofoams at 10 °C / minute ramp rate under nitrogen (blue) and air (red). Samples were deposited with nickel electroless solution for 30 mins then washed with mH<sub>2</sub>O and ethanol before air drying at room temperature.

## 8. Double layer capacitance

Double layer capacitance was utilized to determine the surface area of copper nanofoams by comparing capacitance of 3 bio-templated nanofoams to that of a standard Cu electrode with surface area  $0.9\text{cm}^2$  and AFM measured roughness of 1.01. Conditions utilized included 1 M  $\text{NaClO}_4$ , Ar sparge,  $\text{Hg}/\text{HgSO}_4:\text{KCl}$  reference, 0.658 V vs NHE, DLC at 5 - 50 mV/s at -1.05 V, +/- 0.05 V. A -1.6 V pre-reduction step was also included to ensure that all measured surfaces were in the proper oxidation state. After electrochemical measurements, nanofoam masses were determined via ICP via dissolution in .5ml of Aqua Regia. Average geometric surface area of copper nanofoams was measured to be  $0.34\text{cm}^2 \pm 0.01$ .

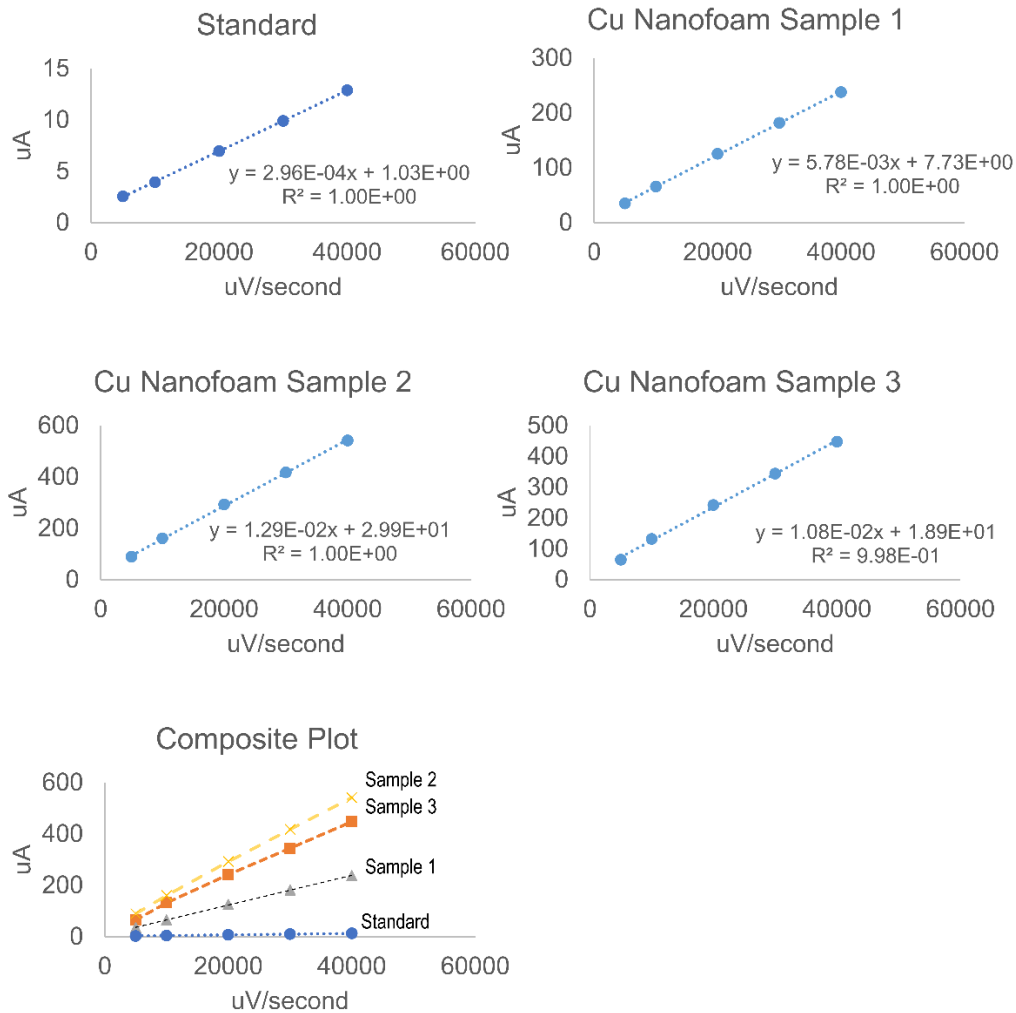


Figure S 15 Double layer capacitance calculations for copper nanofoams and resulting mass normalized surface area

Table S 2 Mass normalized surface area for nickel nanofoam samples

Sample	Mass (mg)	Surface Area (cm <sup>2</sup> )	Mass Normalized SA (m <sup>2</sup> /g)
1	0.553	33.166	4.51
2	0.461	39.6	6.36
3	0.397	17.75	4.47
		Average	5.11 ± 1.08

## 9. Support integration

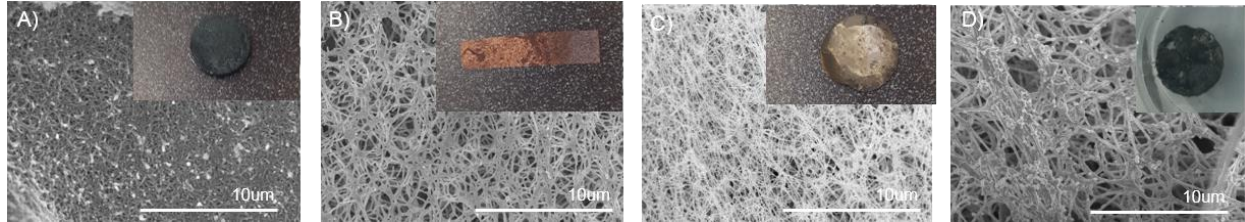


Figure S 16 Retained nanofoam architecture after integration of (A) a nickel nanofoam into a metal foam support (B) copper nanofoam integrated onto a carbon paper support (C) a nickel nanofoam onto a steel mesh (D) a cobalt nanofoam onto silicon filter paper Inset images depict bench scale photograph of resulting samples

## 10. Free standing nanofoam synthesis

Concentrated virus solution was added to a prefabricated mold. 50% Glutaraldehyde was added to each sample, and the samples were allowed to crosslink for 12-18 hours, sensitized, and Nickel was deposited. Monoliths were solvent exchanged into ethanol and dried from CO<sub>2</sub> using critical point drying

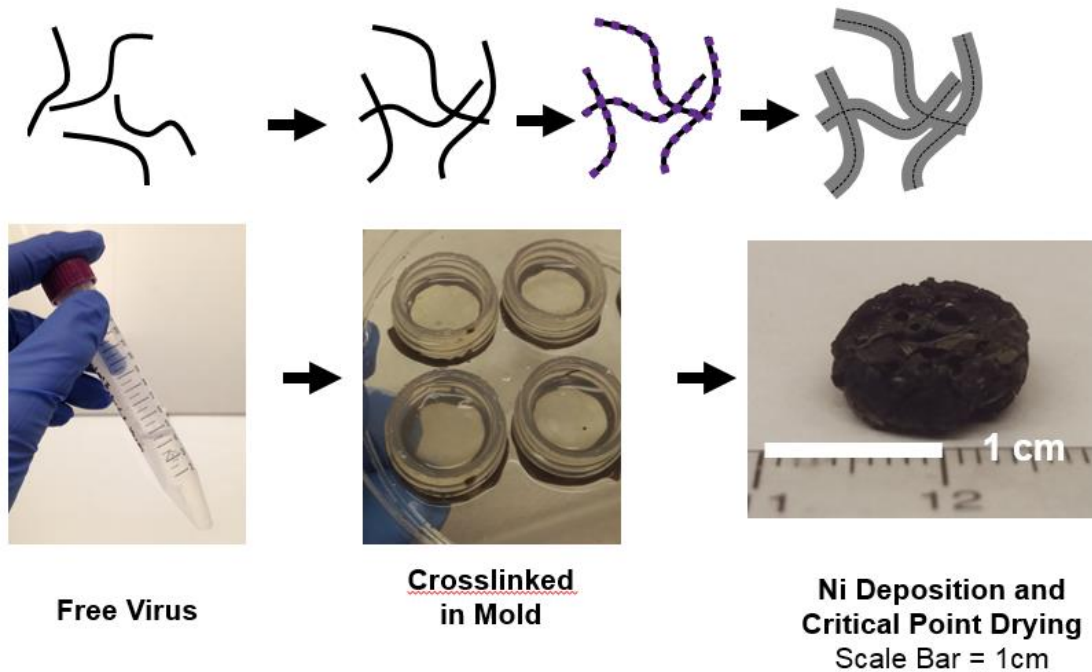


Figure S 17 Freestanding nickel nanofoam synthesis schematic

# 11. Conductivity

**Four-Point Probe Conductivity:** A Keithley 4200-SCS Semiconductor Characterization System was used as a four-point probe to determine resistivity and conductivity of film samples in conjunction with film thicknesses determined from profilometry. The probe head consisted of four tungsten carbide probes 62.5mil (1.5875mm) apart for a total width of 4.7625mm between the outer probes. Current,  $I$ , sweeps of 0.1-100 mV with 20 steps were sourced between the outer probes.

Resistance,  $R$ , was calculated as follows and was verified to obey a linear, ohmic relationship

$$R = \frac{V_{diff}}{I}$$

Sheet resistance,  $R_{sq}$ , was calculated as

$$R_{sq} = \frac{\pi R}{\ln(2)}$$

Thus, film sample resistivity,  $\rho$ , was calculated as:

$$\rho = t * R_{sq} = t * \frac{\pi V_{diff}}{\ln(2) * I}$$

$V_{diff}$  = voltage difference measured between the high impedance middle probes

$I$  = current

$t$  = film thickness determined via profilometry

**Profilometry:** A Veeco DEKTAK 150 Profilometer was used to determine sample thicknesses. A razor blade was used to cut a "Z" at multiple locations along a profile path to assist in leveling the profile during analysis. A step height calibrated 2.5  $\mu\text{m}$  stylus was drawn over the sample with a 2.0-3.0mg force setting at an approximately 200  $\mu\text{m/s}$  scan rate. Average step heights were determined by calculating the difference between average profile height values of the substrate and top of the film surface. Surface roughness values were determined over length scales of greater than 1000  $\mu\text{m}$ .

Table S 3: Nickel nanofoam conductivities in thin film format

Diameter (nm)	Foam thickness ( $\mu\text{m}$ )	$R$ ( $\Omega$ )	$R_{sq}$ ( $\Omega$ )	$\rho$ ( $\Omega\text{m}$ )	Measured $\rho$ / Bulk $\rho$
69.7	6.7	0.649	2.94	19.7E-6	288.0
112.9	10.3	0.126	0.571	5.88E-6	86.0
137.1	6.1	0.104	0.472	2.87E-6	42.0

Table S 4: Copper nanofoam conductivities in thin film format

Diameter (nm)	Foam thickness ( $\mu\text{m}$ )	$R$ ( $\Omega$ )	$R_{sq}$ ( $\Omega$ )	$\rho$ ( $\Omega\text{m}$ )	Measured $\rho$ / Bulk $\rho$
115	10.3	0.0236	0.11	1.10E-6	66.0
139	111.8	0.0200	0.09	1.07E-6	62.7
188	20.9	0.0114	0.05	1.07E-6	63.2

Table S 5: Resistance of common electrode materials<sup>4</sup>

Material	$\rho$ ( $\Omega\text{m}$ )
Bulk nickel	6.40E-8
Bulk copper, annealed	1.68E-8
Amorphous carbon	5E-4 to 8E-4
Graphite	2.5E-6 to 5E-6 parallel plane 3E-3 perpendicular plane

## 12. Catalytic behavior of M13 derived nanofoams

**Electrode fabrication:** Disks of carbon (graphite rod Alfa Aesar ultra "F" purity) polished successively with (Thor Labs LF5P- LF1P). 8 ul of M13 bacteriophage at a concentration of  $10 \times 10^{12}$ - $100 \times 10^{12}$  was placed on the surface of the disk. The disk was then inverted in glutaraldehyde, template side face down and allowed to crosslink for 30 minutes. After 12-24 hours of dialysis in DI water, the sample was placed in 10mM tetraminepalladium chloride solution (Aldrich 99.99%) for a minimum of 6 hours before a second dialysis in DI water for 12-24 hours. Samples were removed from the DI water and then, under a bench top vacuum, samples were submerged in 1 mL of a nickel electroless deposition solution described in Chapter 2, section 4. Samples were submerged for 20 minutes for Ni-DMAB and 40 minutes for Ni-Sodium Hypophosphate solutions. After deposition, samples were rinsed in DI water for 20 minutes on a bench top shaker before drying overnight in a bench top vacuum. Dried samples were adhered to stainless steel wire (which had undergone rolling to provide a flat surface) with silver paint. The metal wire, silver paint, and remaining graphite surfaces were then masked with paraffin wax (sigma aldrich). Wax was heated to 80 °C and painted on to the surfaces to be masked.

Control samples were fabricated by the same method described previously, without 8 ul of M13 bacteriophage dropped onto the surface before processing. Initial tests of both non-templated controls and templated Nickel were fabricated inside carbon paper, also according to the previously described method utilizing a 2cm x 0.3cm strip of carbon paper instead of a graphite support (Toray carbon paper TGP-H-60). Additionally, before electrode preparation, all carbon paper was activated via handheld blowtorch for 30 seconds.

**Electrochemical testing:** Electrochemical testing was carried out utilizing a Bio-Logic VSP-300. All solvents were sparged with argon for one hour before commencing electrochemical measurements as well as during the electrochemical measurements. All measurements were performed at ambient temperature under stirring. All cells were cleaned with alconox followed by sonication in Millipore water for 1 hour. Ag/AgCl reference electrodes (EXAQ and BASi, MF-2078) were utilized for all tests unless otherwise noted along with a high surface area Pt-mesh counter electrode (Alfa Aesar, 99.997%). Ag/AgCl reference electrodes were stored in distilled water between measurements and were checked periodically against pristine references to ensure usage suitability. Uncompensated cell resistance was measured at the start of each experiment utilizing the impedance spectroscopy test function in the BioLogic software and in situ iRu compensation was set to 80 % of the measured Ru values. Data was analyzed via EC-lab.

Glycerol oxidation measurements were taken utilizing 50mL of 0.1M glycerol (Aldrich >99%), 0.1 M NaOH (aldrich) freshly prepared from 1 M stocks of both glycerol and NaOH into millipore water. Measurements were taken in a 100mL 3-necked round bottom flask. Cyclic voltammetry was measured for a minimum of 40 cycles per sample and at the scan rate of 5 mV/sec unless otherwise noted. All measurements were taken with n=2 on two separate days.

Nickel templated EEAE clones were tested for glycerol oxidation activity (Figure S 13). While oxidation-reduction corresponding to nickel hydroxide formation is observed in the 0.1 M NaOH cyclic voltammetry, a large oxidation peak is observed in the presence of both 0.1 M glycerol and 0.1 M NaOH. Compared to non-templated nickel controls, on both carbon paper and graphite disks, the templated nickel exhibited greater current densities and lower onset potentials. As demonstrated by extracts of the 9<sup>th</sup> cycle (Figure S13 panels B and C).

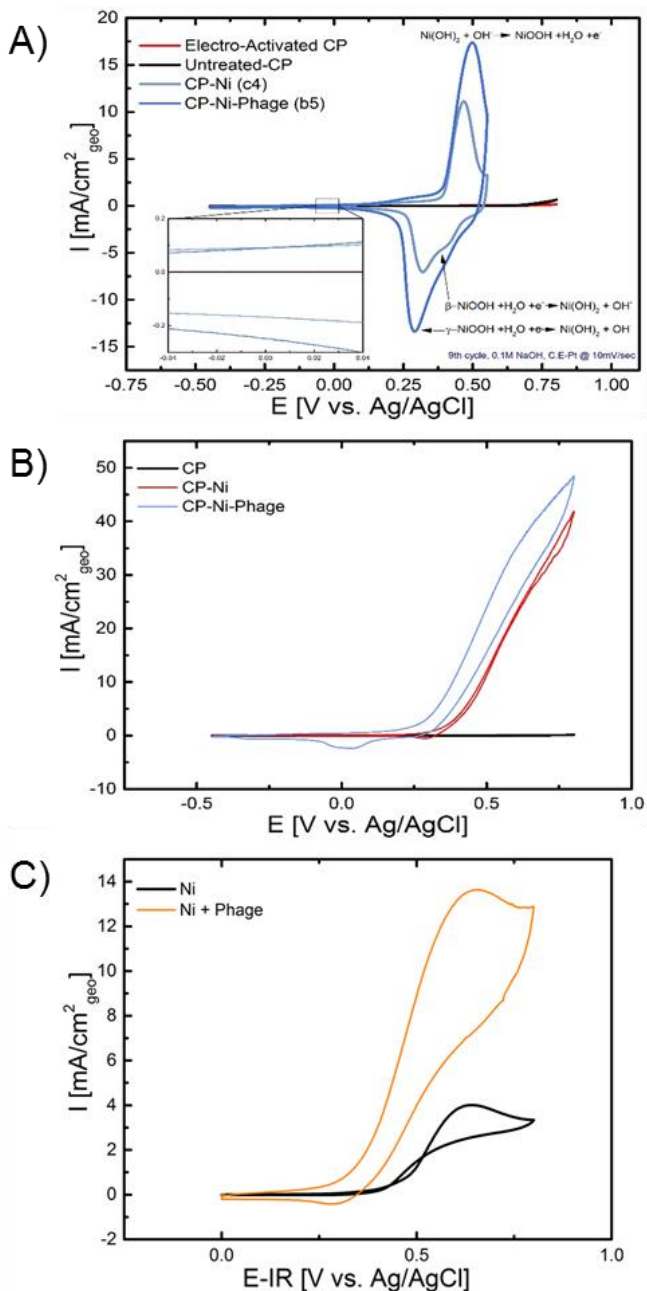


Figure S 18: M13 templated nanofoams catalyze glycerol oxidation (A) cyclic voltammogram of templated and non-templated nickel on carbon paper in 0.1M NaOH only. Peaks are labeled with suggested oxidation reactions (B) cyclic voltammogram of templated nickel and controls on carbon paper in 0.1 M Glycerol and 0.1 M NaOH (C) cyclic voltammogram of templated nickel and controls on graphite disk in 0.1 M Glycerol and 0.1 M NaOH

Electrodes fabricated with the clone ETSYFYDT (green) demonstrated a significant increase in onset potential as compared to electrodes fabricated with EEAE (blue).

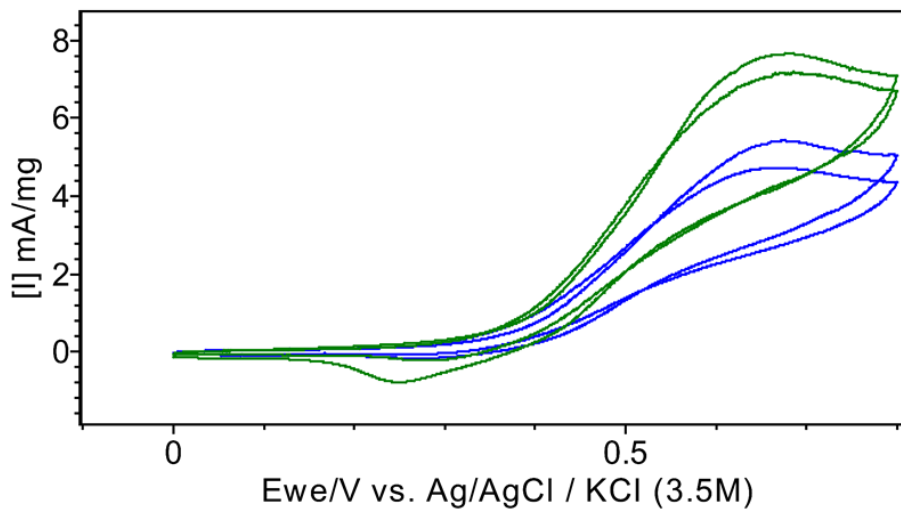
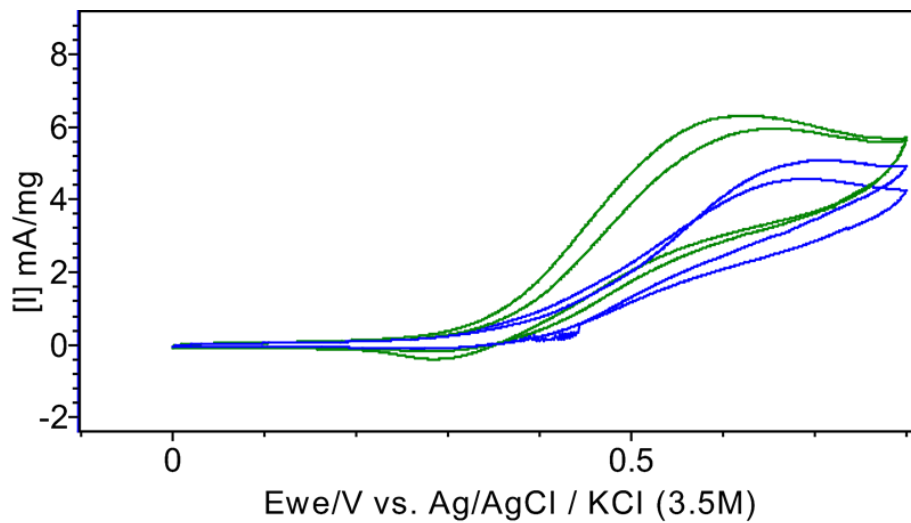


Figure S 19 Template protein affects maximum current density and onset potential in glycerol oxidation reaction. Cyclic voltammograms of nanofoams in 0.1 M glycerol and 0.1 M NaOH. Replicate nanofoams synthesized with the clone ETSYFYDT (green) and EEAE (blue) fabricated at templating concentrations of  $6 \times 10^{13}$  (top) and  $4 \times 10^{13}$  (bottom).

## Supplement references

1. Casey, J. P., Barbero, R. J., Heldman, N. & Belcher, A. M. Versatile de Novo Enzyme Activity in Capsid Proteins from an Engineered M13 Bacteriophage Library. *J. Am. Chem. Soc.* **136**, 16508–16514 (2014).
2. Huang, Y. *et al.* Programmable Assembly of Nanoarchitectures Using Genetically Engineered Viruses. doi:10.1021/nl050795d
3. Belcher, A. M., Engineering, B., Supervisor, T. & Schuh, C. A. M13 virus / single-walled carbon nanotubes as a materials platform for energy devices and biomedical applications M13 virus / single-walled carbon nanotubes as a materials platform for energy devices and biomedical applications. (2011).
4. MatWeb: Material Property Data. Available at:  
<http://www.matweb.com/search/DataSheet.aspx?MatGUID=9aebe83845c04c1db5126fada6f76f7e>.